Supplementary Information

High resolution photonic force microscopy based on sharp nano-fabricated tips

Rudy Desgarceaux*[1,4], Zhanna Santybayeva*[1], Eliana Battistella[1], Ashley L. Nord[1], Catherine Braun-Breton[2], Manouk Abkarian[1], Onofrio M. Maragò[3], Benoit Charlot[†4], and Francesco Pedaci[†1]

[1]CBS Un.Montpellier, CNRS, INSERM, Montpellier, France
[2]Un.Montpellier, CNRS UMR 5235, Montpellier, France
[3]CNR-IPCF, Istituto per i Processi Chimico-Fisici, Messina, Italy
[4]IES, CNRS UMR 5214, University of Montpellier, Montpellier, France
*equal contribution
†corresponding authors

Contents

1 Methods

1.1 Nanofabrication protocol

The nanofabrication process is depicted in fig.1a and SI fig.4. One 4-inch x-cut single crystal quartz wafer is diced into 2x2 cm^2 chips using a dicing saw (DAD 3200, Disco, Japan). The substrate is cleaned with a Piranha solution (3:1 mixture of sulfuric acid (H_2SO_4) and hydrogen peroxide (H_2O_2)) and covered with 0.8 μm thick silicon dioxide deposited by Plasma Enhanced Chemical Vapour Deposition (PECVD) at 280°C using a Corial D200 machine (Corial, France). Next, a 60 nm thick layer of chromium is deposited by electron gun evaporation (Univex 450, Leybold, Germany) on the whole surface. This layer acts as a hard mask for the subsequent plasma etching steps. On these materials stack, we spin-coated a thin layer of AZ 701 MIR photoresist (Merck Performance Materials GmbH, Germany) at 4000 rpm for 30 s, followed by soft baking at 95°C for 1 min. The photoresist is diluted (2:1) to achieve a final thickness of 600 nm.

The quartz sample is then exposed by Laser Interference Lithography, as detailed in [1]. Briefly, this mask-less technique uses subsequent laser exposures with interference fringes to produce a 2D array of dots on the sample (fig.1b). A divergent 405 nm laser beam strikes two adjacent mirrors facing each other at an angle θ, creating two beams interfering at the plane of the photoresist-coated sample. A first exposure (of duration 130 s) imprints on the photoresist a set of parallel lines whose spatial period is 1.8 μm. In order to obtain an array of discs, we proceed with a second exposure with the substrate rotated by 90°. After the exposures, the sample is baked at 110°C for 1 min and developed with AZ 726 developer for 17 s under smooth agitation. The result is an array of discs with a spatial period of 1.8 μm and diameter of 1 μm.

The next step consists in transferring the photoresist pattern onto the quartz substrate. To achieve the high anisotropy required by the cylindrical geometry, we use inductive coupled plasma reactive ion etching (ICP-RIE). The chromium layer is etched with Argon plasma in the absence of oxygen, using a Corial 250D ICP RIE (200 W RF and 400 W LF). The absence of oxygen prevents the photoresist from shrinking during etching, allowing the unprotected Chromium hard mask to be completely removed in 6 min with sufficient selectivity. Etching of the SiO_2 and quartz stack is achieved by a second ICP-RIE process using a mixture of CHF_3 (100 sccm) and O_2 (10 sccm), an internal pressure of 10 mTorr, and an incoming power of 120 W RF and 400 W LF. In these conditions, the etching rate of the quartz is about 100 nm/min. The cylinders obtained are 2.6 μm thick and slightly conical, with a wall angle of about 80 deg (fig.1b, SI fig.4).

In order to create the sharp tips, we use a thinning step by wet etching in hydrofluoric acid (HF), taking advantage of the large difference in etching rate between quartz and SiO_2 (1 and 200 nm/min, respectively [2]). The quartz substrate is entirely dipped in 5% HF during 3 min, and due to the isotropic character of the SiO_2 etching, the profile of the SiO_2 cylinder forms a sharp tip. The remaining chromium discs are then removed by wet etching (in a mixture of perchloric acid (HClO4), and ceric ammonium nitrate (NH4)$_2$[Ce(NO$_3$)$_6$]). The last step consists of mechanically cleaving the particles using a blade (fig.1b). The particles are then collected and stored in aqueous solution.

1.2 Optical setup

The optical tweezers setup, based on the one described in [3], is sketched in fig.1d. We use a linearly polarized infrared laser (1064 nm, 3W Azur Light Systems), whose intensity is adjusted and actively clamped to the suited value (20-60 mW at the objective input) by the combination of one half waveplate, one polarizer, and an acusto-optical modulator driven by a PID controller. The collimated beam is expanded to slightly overfill the back aperture of the microscope objective (Zeiss C-Apochromat 63x/1.2NA, water immersion), via a 1:1 telescope. A water immersion objective was chosen to minimize the z-dependent aberrations of the trap [4]. The laser trap is generated in the liquid medium enclosed in a flow cell, prepared by two glass cover slips separated by one layer of parafilm and sealed. The samples used are positioned on the bottom glass surface. Due to the cylindrical geometry, the particle remains vertical in the trap, with its geometrical axis parallel to the laser propagation direction. The laser trap is linearly polarized, which produces a torque on the birefringent particle [5, 6] that prevents rotation around the geometrical axis. The flowcell position is controlled in three dimensions by a piezo stage with nm resolution (P-517.3CD). The laser trap output is collected by a condenser, identical to the objective, and analyzed by forward-scattering interferometry. To detect the lateral (x, y) displacement of the trapped particle, we use a position sensitive detector (PSD, DL100-7-PCBA3 First sensor Inc.), located on a conjugate plane of the back focal plane of the condenser. In parallel, the axial particle displacement (z) is measured by a photodetector (DET 10N/M, Thorlabs). This allows independent control of the numerical aperture at the two detector planes, maximizing both of their sensitivities (the aperture is maximal for the PSD, while it is reduced by an iris placed on-axis before the photodetector) [7, 8]. The voltage signals of the optical detectors and of the piezo stage are acquired synchronously by a FPGA card at 200-500 kHz (PXI-7852R, National Instruments). The hardware-software interface is developed in Labview, and the following data analysis is performed in Python.

1.3 Sample preparation

Etched glass structures

The sample used in fig.3 consists of structures directly etched onto a 24x60 mm^2 microscope coverslip. Polystyrene micro-beads (100 nm diameter) are deposited on the glass surface by spincoating (2000 rpm for 30 s). A plasma etching reactor (Corial 250D ICP RIE) is used to etch the coverslip, the beads playing the role of a mask. During the scan, passivation of the surfaces is achieved by 10 minutes incubation of bovine serum albumin (BSA) in the flow cell.

Red blood cells

P. falciparum 3D7 strain, obtained from the Malaria Research and Reference Reagent Resource Center (MR4-BEI resources, MRA-102), was cultured in human erythrocytes obtained as donations from anonymized individuals from the French Blood Bank (Etablissement Français du Sang, Pyrénées Méditerranée, France; approval number 21PLER2016-0103) at 5% hematocrit in RPMI 1640 medium (Gibco), supplemented with gentamycin at 20 μg/ml and 10% human serum [9]. The cultures were kept at 37°C under a controlled trigaz atmosphere (5% CO_2 , 5% O_2 and 90% N_2). To minimize knobless parasite mutants under in vitro culture, mature parasites were isolated using gelatin floatation on a weekly basis [10]. The synchronization of the parasites was achieved by

purification of mature parasites on a Variomacs column [11] followed by 5% sorbitol [12] treatment 2hours post-invasion. Mature trophozoites were collected by passage through a VarioMACS column (Miltenyi Biotec; $> 95\%$ infected erythrocytes) and resuspended in complete culture medium under 5% O_2 controlled atmosphere.
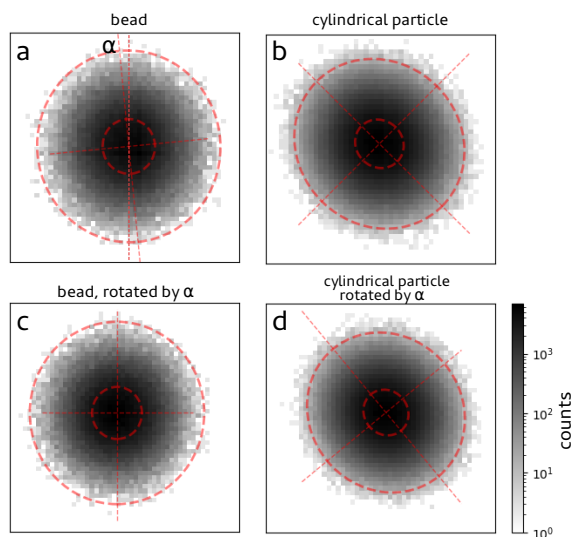
2   Cross talk correction

Figure 1: Distributions of particle positions in the x, y plane and Gaussian fit. **a)** Distribution of points visited in the plane x, y by a 1 μm diameter bead. A two dimensional Gaussian fit finds the widths and angle (here $\alpha_{\text{bead}} = 5.6^o$) of the distribution. **b)** Same for a nanofabricated particle with tip. **c) d)** Corresponding corrections of the cross talk by rotation of $-\alpha_{\text{bead}}$.

To correct for the residual cross talk between the signals S_x and S_y, we proceed as follows. We first quantify the cross talk by trapping a 1 μm diameter bead in bulk. We fit the corresponding points in the S_x, S_y plane by a Gaussian model (based on the expectation-maximization algorithm implemented in python sklearn[1], see fig.1a). The fit provides the two standard deviations (σ_1, σ_2) along the two main axis of the elliptical pattern as well as its angle α_{bead}. Our tests show that a ratio $\sigma_1/\sigma_2 = 1.001$ is detectable by the algorithm, using an order of 10^6 points as in the experiment. For the bead, we find $\sigma_1/\sigma_2 = 1.047$. It is then possible to correct for the cross talk by rotating the points by an angle $-\alpha_{bead}$ (fig.1c). Trapping a nanofabricated particle, the fit to the probability distribution provides $\sigma_1/\sigma_2 = 1.087$ (fig.1b), and an angle α_{cyl} larger than α_{bead}. The final distribution of points for the nanofabricated particle, corrected by the angle α_{bead} is shown in SI fig.1d.

3   Correlation analysis

Following the works that analysed the behavior of elongated and cylindrical nano-particles in optical traps at low Reynolds number [13–15], we can summarize the following results. The Langevin

---

[1]https://scikit-learn.org/stable/modules/mixture.html

equations for the linear displacement of the center of mass (X, Y, Z) and for the angular tilt (Θ_x, Θ_y) can be written as

$$
\begin{aligned}
\partial_t X(t) &= -\omega_x X(t) + \sqrt{2k_B T \gamma_x}\, \xi_x(t) \\
\partial_t Y(t) &= -\omega_y Y(t) + \sqrt{2k_B T \gamma_y}\, \xi_y(t) \\
\partial_t Z(t) &= -\omega_z Z(t) + \sqrt{2k_B T \gamma_z}\, \xi_z(t) \\
\partial_t \Theta_x(t) &= -\Omega_x \Theta_x(t) + \sqrt{2k_B T \gamma_{\Theta_x}}\, \xi_{\Theta_x}(t) \\
\partial_t \Theta_y(t) &= -\Omega_y \Theta_y(t) + \sqrt{2k_B T \gamma_{\Theta_y}}\, \xi_{\Theta_y}(t)
\end{aligned}
\tag{1}
$$

where the rates are defined by

$$
\begin{aligned}
\omega_x &= k_x/\gamma_\perp & \Omega_x &= k_{\Theta_x}/\gamma_{\Theta_x} \\
\omega_y &= k_y/\gamma_\perp & \Omega_y &= k_{\Theta_y}/\gamma_{\Theta_y} \\
\omega_z &= k_z/\gamma_\parallel &&
\end{aligned}
\tag{2}
$$

and where k_i is the stiffness $(i = x, y, z, \Theta_x, \Theta_y)$, $\gamma_\perp, \gamma_\parallel$ are the linear drag coefficients (perpendicular and parallel to the geometrical axis of the particle), $\gamma_{\Theta_x}, \gamma_{\Theta_y}$ are the angular drag coefficients, $\xi_i(t)$ are uncorrelated noise sources, and $k_B T$ is the thermal energy. The (auto and cross) correlation functions for these degrees of freedom can be written [13] in general as

$$
C_{ab}(\tau) = \langle a(t)\, b(t+\tau) \rangle
\tag{3}
$$

where $a, b = (X, Y, Z, \Theta_x, \Theta_y)$. The auto-correlation functions follow the differential equation $\partial_\tau C_{aa}(\tau) = -(k_a/\gamma_a)\, C_{aa}$, with exponentially decaying solution

$$
C_{aa}(\tau) = \langle a(t)\, a(t+\tau) \rangle = \frac{k_B T}{k_a}\, e^{-(k_a/\gamma_a)|\tau|} \qquad a = (X, Y, Z, \Theta_x, \Theta_y).
\tag{4}
$$

where the equipartition theorem implies that

$$
C_{aa}(\tau = 0) = \langle a^2(t) \rangle = var(a) = \frac{k_B T}{k_a} \qquad (a = X, Y, Z, \Theta_x, \Theta_y).
\tag{5}
$$

(note the different units: $[C_{xx,yy,zz}] = m^2$, $[C_{\Theta_{x,y}}] = 1$, $[k_{x,y,z}] = N/m$, $[k_{\Theta_{x,y}}] = Nm$).

In the small tilt angle regime, the calibrated signals S_z, S_x, S_y (already mapped to meters) acquired from the detectors couple together the linear X, Y, Z and the angular Θ_x, Θ_y variables. If L is the length of the particle, it can be written

$$
\begin{aligned}
S_x &= X + L\Theta_x \\
S_y &= Y + L\Theta_y \\
S_z &= Z
\end{aligned}
\tag{6}
$$

The correlation functions of the calibrated acquired *signals* can therefore be written as

$$
C_{xx}(\tau) = \langle X(t)\, X(t+\tau) \rangle + L^2 \langle \Theta_x(t)\, \Theta_x(t+\tau) \rangle
$$

5

$$
\begin{aligned}
C_{yy}(\tau) &= \langle Y(t)\,Y(t+\tau)\rangle + L^2\langle\Theta_y(t)\,\Theta_y(t+\tau)\rangle \\
C_{zz}(\tau) &= \langle Z(t)\,Z(t+\tau)\rangle \\
C_{xy}(\tau) &= L^2\langle\Theta_x(t)\,\Theta_y(t+\tau)\rangle \\
C_{yx}(\tau) &= L^2\langle\Theta_y(t)\,\Theta_x(t+\tau)\rangle
\end{aligned}
\tag{7}
$$

(note the difference in notation between the correlation of the linear physical displacement C_{XX} of eq.3, and the correlation of the corresponding measured signal C_{xx}). Combining eq.1,2,4,7, one can explicitly write the expressions of the correlation functions of the *signals* as

$$
\begin{aligned}
C_{xx}(\tau) &= \frac{k_BT}{k_x}\exp\left[-\frac{k_x}{\gamma_\perp}\tau\right] + L^2\frac{k_BT}{k_{\Theta_x}}\exp\left[-\frac{k_{\Theta_x}}{\gamma_{\Theta_x}}\tau\right] \\
C_{yy}(\tau) &= \frac{k_BT}{k_y}\exp\left[-\frac{k_y}{\gamma_\perp}\tau\right] + L^2\frac{k_BT}{k_{\Theta_y}}\exp\left[-\frac{k_{\Theta_y}}{\gamma_{\Theta_y}}\tau\right] \\
C_{zz}(\tau) &= \frac{k_BT}{k_z}\exp\left[-\frac{k_z}{\gamma_\parallel}\tau\right] \\
C_{xy}(\tau) &= C_{xy}(0)\exp\left[-\frac{k_{\Theta_y}}{\gamma_{\Theta_y}}\tau\right] \\
C_{yx}(\tau) &= C_{yx}(0)\exp\left[-\frac{k_{\Theta_x}}{\gamma_{\Theta_x}}\tau\right]
\end{aligned}
\tag{8}
$$

where $\tau \geq 0$, $C_{xy}(\tau) = C_{yx}(-\tau)$. For $\tau = 0$, now one obtains for x, y a combination of linear and angular displacement:

$$
\begin{aligned}
C_{xx}(0) &= \langle S_x(t)^2\rangle = var(S_x) = \frac{k_BT}{k_x} + L^2\frac{k_BT}{k_{\Theta_x}} \\
C_{yy}(0) &= \langle S_y(t)^2\rangle = var(S_y) = \frac{k_BT}{k_y} + L^2\frac{k_BT}{k_{\Theta_y}}
\end{aligned}
\tag{9}
$$

We note the following: 1) experimentally (see fig.2d), we find that all the above correlation functions can be fit by a single exponential. The single-exponential rate of C_{xx}, C_{yy}, and C_{xy} are equal (within 3%). 2) from the exponential fit of C_{xy} and C_{yx}, we find $\Omega_x = \Omega_y = \Omega = 5030\,\frac{1}{\text{s}}$ (within 0.6%). We can set $\gamma_\Theta = \gamma_{\Theta_x} = \gamma_{\Theta_y}$, so it results $k_\Theta = k_{\Theta_x} = k_{\Theta_y}$. Because C_{xx} and C_{yy} are very similar, we can set $C_\perp = C_{xx} = C_{yy}$, and $\omega_x = \omega_y$, so $k_\perp = k_x = k_y$. We call $C_\parallel = C_{zz}$, and $k_z = k_\parallel$. Therefore we can write a simplified version of eq.8 as

$$
\begin{aligned}
C_\perp(\tau) &= \frac{k_BT}{k_\perp}\exp\left[-\frac{k_\perp}{\gamma_\perp}\tau\right] + \frac{k_BT}{k_\Theta}L^2\exp\left[-\frac{k_\Theta}{\gamma_\Theta}\tau\right] \\
C_\parallel(\tau) &= \frac{k_BT}{k_\parallel}\exp\left[-\frac{k_\parallel}{\gamma_\parallel}\tau\right] \\
C_{xy}(\tau) &= C_{xy}(0)\exp\left[-\frac{k_\Theta}{\gamma_\Theta}\tau\right]
\end{aligned}
\tag{10}
$$

We now calculate the theoretical values of the drag coefficients for a cylinder with length L and diameter d similar to our particle ($L = 1.2 - 1.7\,\mu$m, $d = 0.7 - 1.2\,\mu$m, see SI sec.4):

$$
\begin{aligned}
\gamma_\parallel &= (8.8 \pm 1.9)\,10^{-6}\ \text{pN s/nm} \\
\gamma_\perp &= (1.4 \pm 0.3)\,10^{-5}\ \text{pN s/nm}
\end{aligned}
$$

$$\gamma_\Theta \quad = \quad 8.81 \text{ pN nm s} \tag{11}$$

From the value of $\Omega = \frac{k_\Theta}{\gamma_\Theta} = 4530\,s^{-1}$, we can estimate $k_\Theta = 4\,10^4$ pN nm. The variance of the tilt angular fluctuations is given by $\sigma_\Theta^2 = \frac{k_B T}{k_\Theta} L^2$, corresponding to an angle $\sigma_\Theta/L = \sqrt{\frac{k_B T}{k_\Theta}} \sim 0.01$ rad (0.6 degrees).
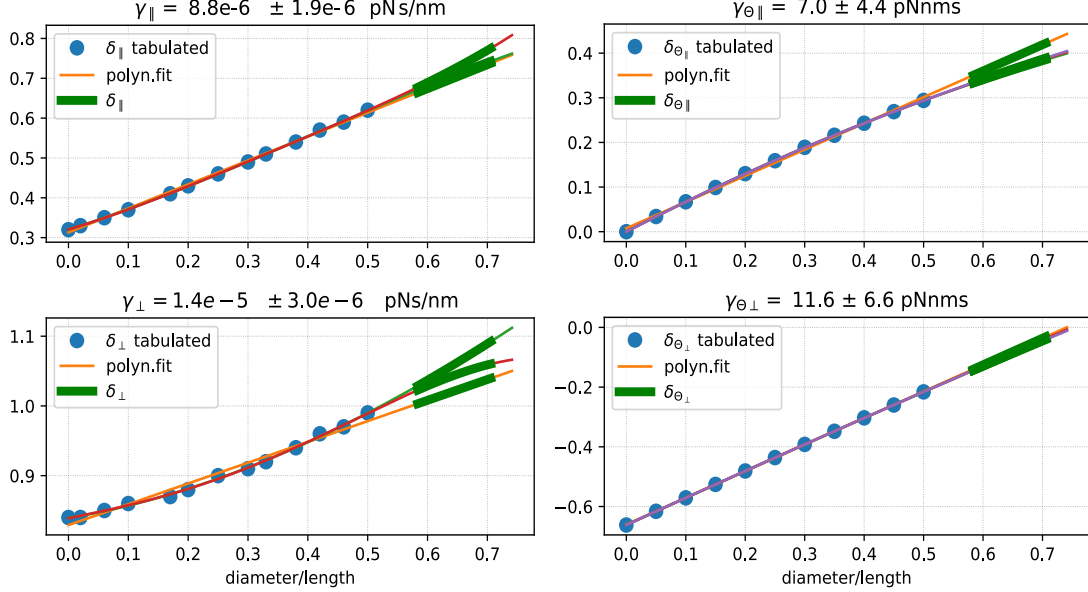
4 Theoretical drag of microscopic cylinders

Figure 2: Values of the parameters δ_i $(i = \perp, \|, \Theta_\perp, \Theta_\|)$ used to calculate the theoretical drag coefficients for cylinders of different diameter and length. The particles used in this work lay in the region marked in green. The tabulated values [16] are shown as blue dots, while their polynomial fits (with order 1 to 4) with lines. In each panel the title indicates the corresponding value of the drag γ_i.

We use the results of [16] to calculate the theoretical values of the drag coefficients of a cylinder of length L and diameter d

$$\begin{aligned}
\gamma_\perp &= \frac{4\pi\eta L}{\ln p + \delta_\perp} \\
\gamma_\| &= \frac{2\pi\eta L}{\ln p + \delta_\|} \\
\gamma_{\Theta_\perp} &= \frac{\pi\eta L^3}{3\left(\ln p + \delta_{\Theta_\perp}\right)} \\
\gamma_{\Theta_\|} &= 3.841\,\pi\eta L(d/2)^2(1 + \delta_{\Theta_\|})
\end{aligned} \tag{12}$$

where $\gamma_\perp$ and $\gamma_\|$ are the transverse and axial linear translational drag coefficients respectively, $\gamma_{\Theta_\perp}$ and $\gamma_{\Theta_\|}$ are the rotational drag coefficients for a rotation around an axis perpendicular and parallel to the symmetry axis respectively (note that we do not employ here $\gamma_{\Theta_\|}$, which is given just for

7

completeness), η is the water dynamic viscosity, and $p = L/d$. The correction factors $\delta_\perp, \delta_\parallel, \delta_{\Theta_\perp}, \delta_{\Theta_\parallel}$ are tabulated in [16] and plotted in SI fig.2, where their values are fit by polynomial expressions of different order (1 to 4). The region corresponding to a cylinder of dimensions compatible with our particles requires extrapolation the theoretical values by means of the fit, and is marked in green in the plots. The average and standard deviation of the corresponding drag coefficients γ_i are indicated in each plot and used in eq.11.
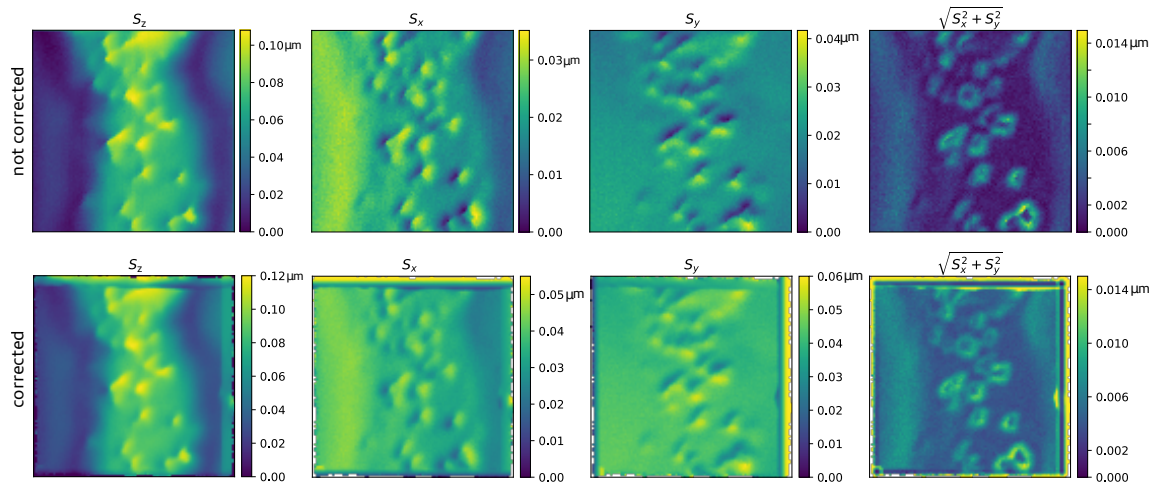
5 Calibration and image reconstruction

Figure 3: Images from the acquired signals. Each column corresponds to the images obtained from the calibrated signals S_z, S_x, S_y, and $\sqrt{S_x^2 + S_y^2}$, as labeled on each panel (same data as in fig.3f). The latter is the calculated radial displacement map of the trapped particle, relative to the center of the scanning trap. The first row shows the raw data, while the second row shows the pixel-corrected images, where the transverse displacement of the tip at each pixel is considered to correct the trap transverse position. The images are not high-pass filtered.

An image acquisition starts with the calibration of the particle that will be employed for the scan. This consists initially of a few axial position-displacement curves on bare glass with the two particle configurations in order to discern the presence and orientation of the tip (briefly blocking the laser between the measurements allows us to obtain both tip up and tip down). Secondly, the traces are recorded with the particle in the liquid bulk to obtain the power spectral densities (PSD) of the signals (and optionally the correlations and Allan variance), which are fit by Lorentzian functions. The position-displacement curve is used to quantify the z-sensitivity (β_z), while the fit of the PSD of S_z provides the other two independent measurements to obtain the stiffness k_z and drag γ_z. For the transverse directions x and y, we rely on the theoretical value of the drag of a cylinder $\gamma_\perp$, setting $\gamma_x = \gamma_y = \gamma_\perp$. The PSDs of the signals S_x, S_y then provide the stiffness k_x, k_y and sensitivity β_x, β_y. Once the drag, stiffness, and sensitivity are obtained for the three directions, the signals S_z, S_x, S_y can be mapped to meters and the force can be quantified [17].

To produce an image, we first define the movement of the sample by the piezo stage (we mainly use 100 steps of 10 or 20 nm in both x and y, while z remains constant) and start the scan with the particle in contact to the sample surface. During the scan, we further acquire from the piezo-

driver three voltage signals, which can be converted to nm, and which provide the relative position $x_p(t), y_p(t), z_p(t)$ between the moving sample and the fixed optical trap at each time t ($z_p(t)$ remains constant during the scan). The image of the axial displacement of the particle in the trap (signal S_z) can then be formed by the set of points $(x_p(t), y_p(t), S_z(t))$, while the images of the transverse displacements (S_x, S_y) can be formed by the set of points $(x_p(t), y_p(t), S_x(t))$ and $(x_p(t), y_p(t), S_y(t))$ (see SI fig.3). The points $x_p(t), y_p(t)$ are arranged on a square grid defined by the piezo stage, and can therefore be easily pixelized (each pixel having a surface of 10x10 or 20x20 nm^2). This means that all the $x_p(t), y_p(t)$ points belonging to the same pixel are clustered together and the average (or median) value of their corresponding signal ($S_z(t), S_x(t), S_y(t)$ or $\sqrt{S_x^2 + S_y^2}$) is calculated and used to set the value of the pixel, rendered in a color code.

Once the signals S_x and S_y are calibrated and converted to nm, this information can be used to correct the position $x_p(t), y_p(t)$ of the trap on the sample to reflect the actual x, y position of the tip in the trap, before the pixels are defined. To do so, we simply add the signals S_x, S_y (in nm) to the signals $x_p(t), y_p(t)$ (in nm), and then we pixelize the points as above. Given that S_x and S_y encode maximum transverse displacements of 1 pixel (10-14 nm, see fig.SI3), we find that this correction modifies only slightly the final image. However it is interesting to note how the image of the radial displacement of the tip (signal $\sqrt{S_x^2 + S_y^2}$, see last columns of SI fig.3) underlines the contour of each object in the sample.
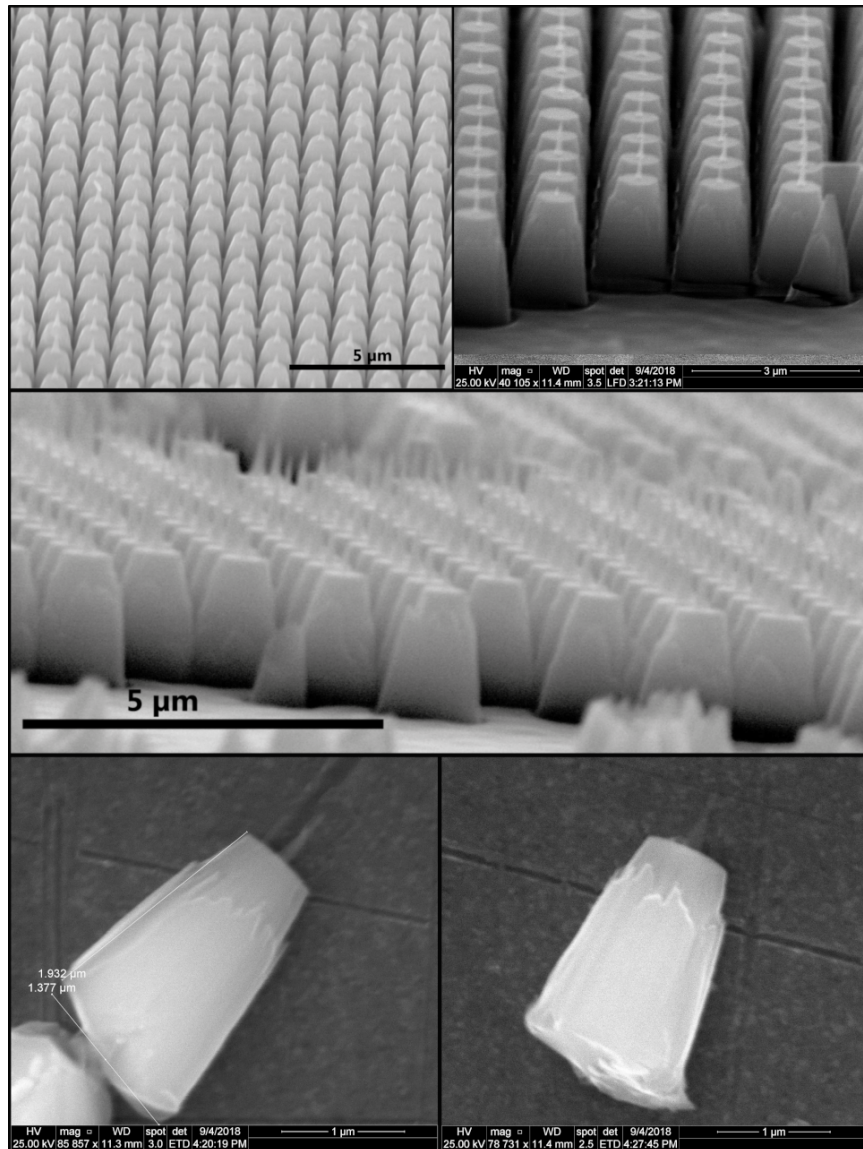
6 Supplementary figures

Figure 4: SEM images of the particles at the end of the nanofabrication process, before and after cleavage.
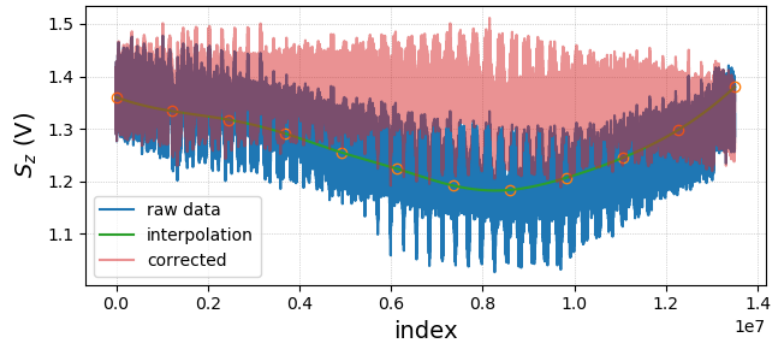
Figure 5: Drift correction on the flatten version of the image. To remove the low frequency content due to the drift during the acquisition in the image, the flatten image (raw data, blue) is interpolated by cubic spline (points and green line). This interpolation is then subtracted from the raw data (corrected, red).
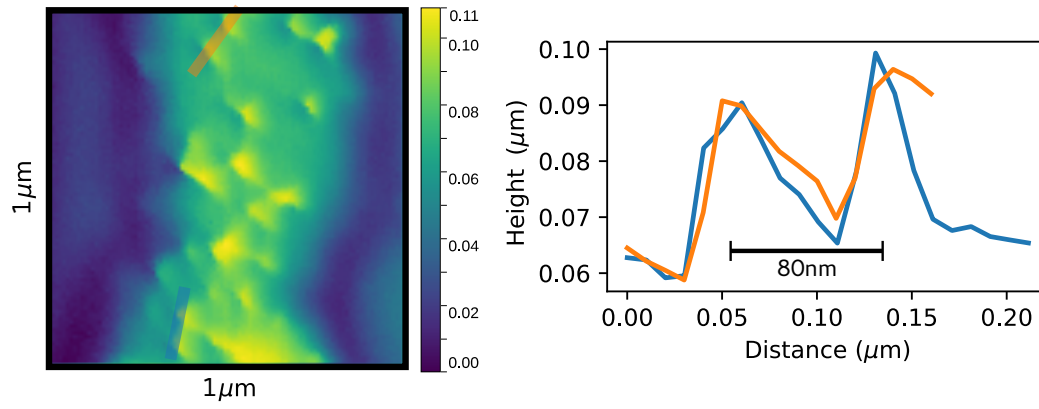
Figure 6: Two height profiles (right) are extracted at the respective positions indicated by the colored bars in the image (left) of the glass etched structures (as in fig.3f).
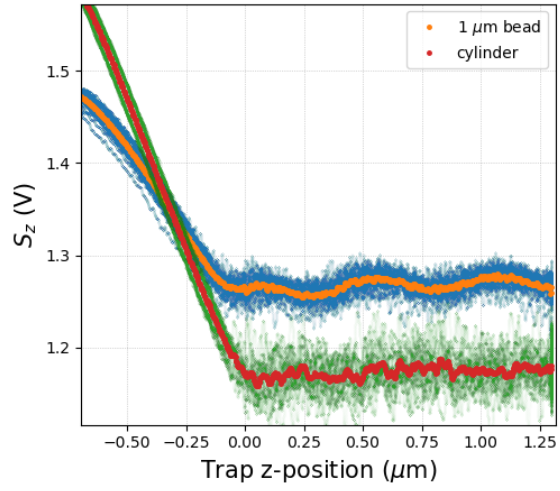
Figure 7: Comparison between the position-displacement curves obtained with a 1 μm polystyrene bead and one cylindrical particle. The oscillations of S_z resolvable with the bead in the trap approaching the glass surface, due to interference with the scattered light [18], are not present in the case of our cylindrical particles.
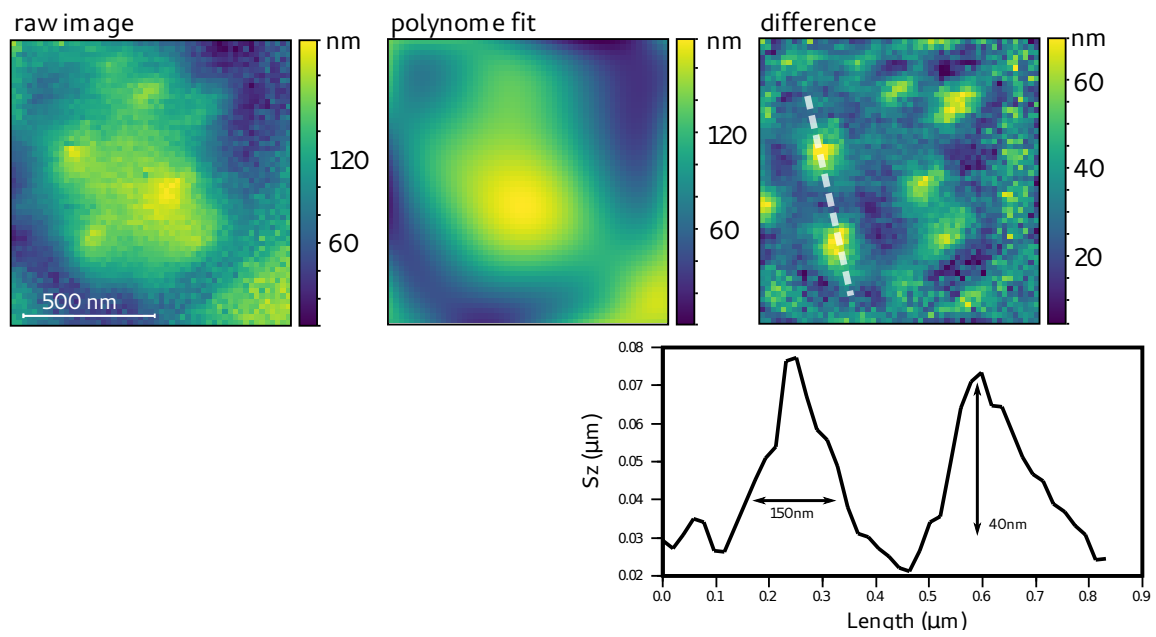
Figure 8: Image filtering procedure. The raw image (same as fig.4e) is fit by a 2D polynomial function (degree 5 here) to obtain the low frequency content. The high-pass filtered image is found by the difference between the fit and the original image. The profile of the knobs along the dashed line is shown in the lower panel.
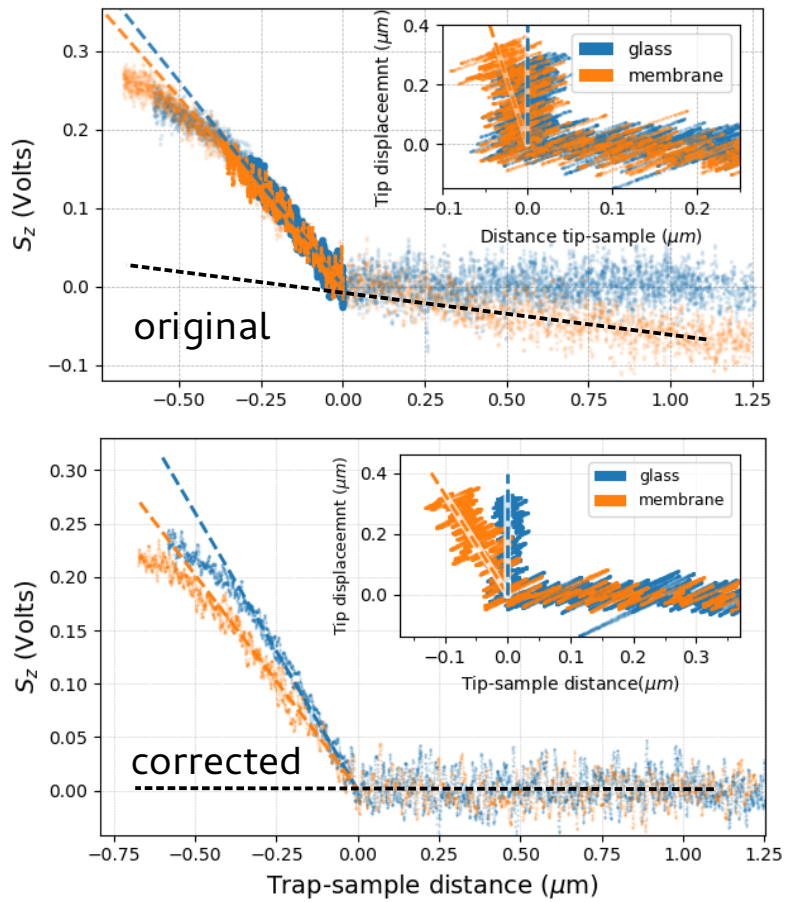
Figure 9: Correction applied to the indentation measurement of the infected red blood cell. Top: due to scattering from the cell, the original S_z curve obtained approaching the optical trap to the membrane (orange) displays systematically a tilt (dashed line) in the region where the trap is far from the membrane surface. Bottom: (same as fig.4b in the main text) the tilt is corrected by subtraction.
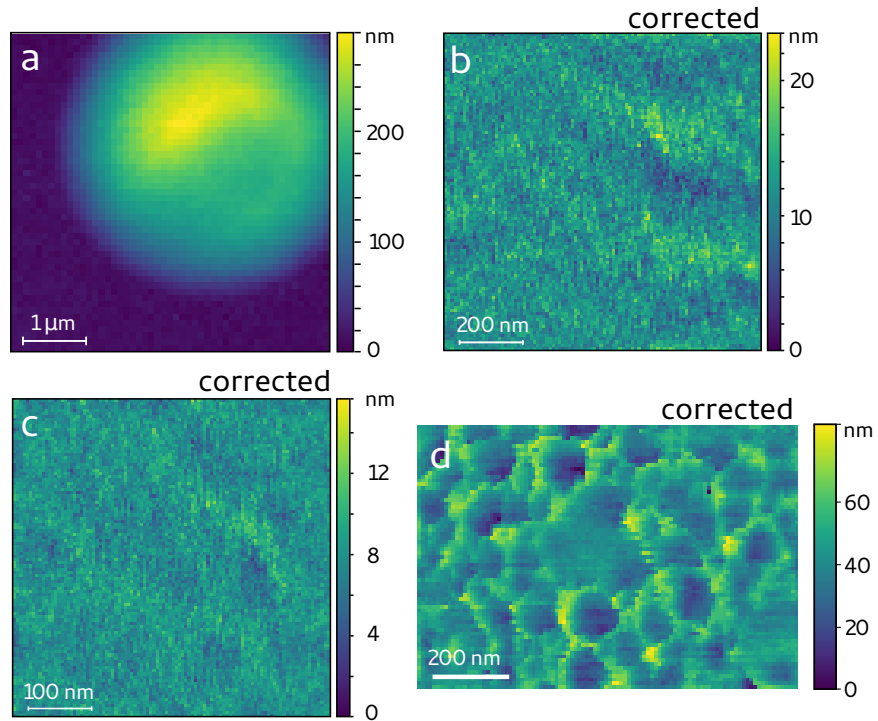
15

Figure 10: Images of non-infected red blood cells. The cells are prepared as ghosts [19] to exchange their optically thick hemoglobin content with external buffer. Their global structure is otherwise unchanged. They are immobilized by PLL coating on the glass coverslip, which builds tension on the membrane and deforms the normal bi-concave conformation of the cell into a dome-shape. Each image corresponds to a different cell. **a)** The 5x5 μm^2 region shows the top part of the cell. The image is formed from the uncorrected S_z calibrated signal. **b)** Corrected (high pass filtered) scan of 1x1 μm^2, **c)** Corrected scan of 0.5x0.5 μm^2. **d)** A particular case of a scan of a red blood cell with structures that we could not easily see on other cells. We speculate that the valleys (darker regions) observed here could correspond to regions of the membrane between the cytoskeleton network, which holds the membrane on the cytosolic side, and which could become visible in a narrow region of the membrane tension applied by PLL. In any case, these structures are clearly different from the knobs of infected cells shown in fig.4.

References

1. Santybayeva, Z. *et al.* Fabrication of quartz microcylinders by laser interference lithography for angular optical tweezers. *Journal of Micro/Nanolithography, MEMS, and MOEMS* **15,** 034507 (2016).

2. Williams, K. R., Gupta, K. & Wasilik, M. Etch rates for micromachining processing-Part II. *Journal of microelectromechanical systems* **12,** 761–778 (2003).

3. Santybayeva, Z. & Pedaci, F. in *Optical Tweezers* 157–181 (Springer, 2017).

4. Vermeulen, K. C., Wuite, G. J., Stienen, G. J. & Schmidt, C. F. Optical trap stiffness in the presence and absence of spherical aberrations. *Applied optics* **45,** 1812–1819 (2006).

5. La Porta, A. & Wang, M. D. Optical torque wrench: angular trapping, rotation, and torque detection of quartz microparticles. *Physical review letters* **92,** 190801 (2004).

6. Pedaci, F. *et al.* Excitable particles in an optical torque wrench. *Nat.Phys.* **7,** 259 (2011).

7. Dreyer, J. K., Berg-Sørensen, K. & Oddershede, L. Improved axial position detection in optical tweezers measurements. *Applied Optics* **43,** 1991–1995 (2004).

8. Rohrbach, A., Kress, H. & Stelzer, E. H. Three-dimensional tracking of small spheres in focused laser beams: influence of the detection angular aperture. *Optics letters* **28,** 411–413 (2003).

9. Trager, W. & Jensen, J. B. Human malaria parasites in continuous culture. *Science* **193,** 673–675 (1976).

10. Pasvol, G., Wilson, R., Smalley, M., Brown, J., *et al.* Separation of viable schizont-infected red cells of Plasmodium faiciparum from human blood. *Annals of tropical medicine and parasitology* **72,** 87–88 (1978).

11. Mata-Cantero, L., Lafuente, M. J., Sanz, L. & Rodriguez, M. S. Magnetic isolation of Plasmodium falciparum schizonts iRBCs to generate a high parasitaemia and synchronized in vitro culture. *Malaria journal* **13,** 112 (2014).

12. Lambros, C. & Vanderberg, J. P. Synchronization of Plasmodium falciparum erythrocytic stages in culture. *The Journal of parasitology,* 418–420 (1979).

13. Volpe, G. & Petrov, D. Torque detection using Brownian fluctuations. *Physical review letters* **97,** 210603 (2006).

14. Marago, O. *et al.* Femtonewton force sensing with optically trapped nanotubes. *Nano letters* **8,** 3211–3216 (2008).

15. Irrera, A. *et al.* Size-scaling in optical trapping of silicon nanowires. *Nano letters* **11,** 4879–4884 (2011).

16. Tirado, M. M. & de la Torre, J. G. Translational friction coefficients of rigid, symmetric top macromolecules. Application to circular cylinders. *The Journal of chemical physics* **71,** 2581–2587 (1979).

17. Berg-Sørensen, K. & Flyvbjerg, H. Power spectrum analysis for optical tweezers. *Review of Scientific Instruments* **75,** 594–612 (2004).

18. Neuman, K. C., Abbondanzieri, E. A. & Block, S. M. Measurement of the effective focal shift in an optical trap. *Optics letters* **30,** 1318–1320 (2005).

19. Schwoch, G. & Passow, H. Preparation and properties of human erythrocyte ghosts. *Molecular and cellular biochemistry* **2,** 197–218 (1973).